

Hydroxylation Catalysis by Mononuclear and Dinuclear Iron Oxo Catalysts: a Methane Monooxygenase Model System versus the Fenton Reagent $\text{Fe}^{\text{IV}}\text{O}(\text{H}_2\text{O})_5^{2+}$

G. Gopakumar,[†] Paola Belanzoni,[‡] and Evert Jan Baerends^{*,†,§,⊥}

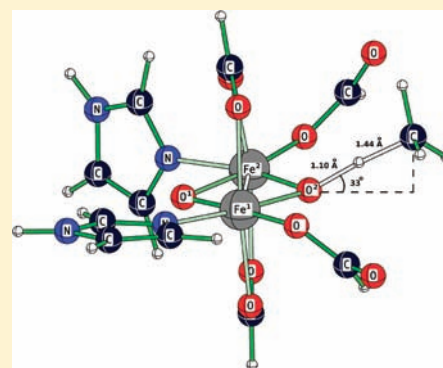
[†]Theoretische Chemie, Vrije Universiteit Amsterdam, De Boelelaan 1083, 1081 HV Amsterdam, The Netherlands

[‡]Department of Chemistry, University of Perugia, via Elce di Sotto 8, 06123 Perugia, Italy

[§]Department of Chemistry, Pohang University of Science and Technology, San 31, Hyojadong, Namgu, 790-784 Pohang, South Korea

[⊥]Department of Chemistry, Faculty of Science, King Abdulaziz University, Jeddah 25189, Saudi Arabia

ABSTRACT: Hydroxylation of aliphatic C–H bonds is a chemically and biologically important reaction, which is catalyzed by the oxidoiron group FeO^{2+} in both mononuclear (heme and nonheme) and dinuclear complexes. We investigate the similarities and dissimilarities of the action of the FeO^{2+} group in these two configurations, using the Fenton-type reagent [FeO^{2+} in a water solution, $\text{FeO}(\text{H}_2\text{O})_5^{2+}$] and a model system for the methane monooxygenase (MMO) enzyme as representatives. The high-valent iron oxo intermediate MMOH_Q (compound Q) is regarded as the active species in methane oxidation. We show that the electronic structure of compound Q can be understood as a dimer of two $\text{Fe}^{\text{IV}}\text{O}^{2+}$ units. This implies that the insights from the past years in the oxidative action of this ubiquitous moiety in oxidation catalysis can be applied immediately to MMOH_Q . Electronically the dinuclear system is not fundamentally different from the mononuclear system. However, there is an important difference of MMOH_Q from $\text{FeO}(\text{H}_2\text{O})_5^{2+}$: the largest contribution to the transition state (TS) barrier in the case of MMOH_Q is not the activation strain (which is in this case the energy for the C–H bond lengthening to the TS value), but it is the steric hindrance of the incoming CH_4 with the ligands representing glutamate residues. The importance of the steric factor in the dinuclear system suggests that it may be exploited, through variation in the ligand framework, to build a synthetic oxidation catalyst with the desired selectivity for the methane substrate.



1. INTRODUCTION

The mononuclear iron(IV) oxo FeO^{2+} (ferryl ion) is well established as the active center in heme iron enzymes such as cytochrome P450.^{1,2} It is also considered as the reactive species in some nonheme enzymes,³ biomimetic complexes,⁴ and in the Fenton reaction.⁵ Although also FeO^+ has been considered as the active species in hydroxylation catalysis with the Fe-ZSM-5 zeolite,^{6a,b} it has recently been argued that FeO^{2+} could very well be the active species (“ α -oxygen”) in the zeolite case.^{6c} The ability of the FeO^{2+} moiety to promote hydrogen abstraction is directly related to its high electrophilicity, which originates from its electronic structure.⁷ The scission of the very stable C–H bond is stimulated by an electron transfer from this C–H bond into a low-lying empty acceptor molecular orbital (MO) of the FeO^{2+} unit. This low-lying empty acceptor orbital is not necessarily the lowest unoccupied molecular orbital (LUMO). In the case of FeO^{2+} in a weak ligand field (as generated by water ligands), the primary acceptor orbital is a low-lying vacant σ^* orbital that accepts electron density from the aliphatic C–H bond. The reactivities of metal oxo species with metals other than iron have been related to the energy, type, and shape (σ^* vs π^*) of the lowest effective acceptor

orbital and the “d” count of the metal.⁸ The overall spin state is also important.^{9,10c} It has been shown that the spin state is controlled by the strength of the equatorial ligand field through differential destabilization of the two δ orbitals, $d_{x^2-y^2}$ and d_{xy} . The high-spin (HS) state is favorable for the action of FeO^{2+} as an electron acceptor because the stabilizing exchange field of the excess α spin electrons lowers the energy of the primary acceptor orbital of the α spin. However, it is not just a HS state that is important. There certainly is an exchange stabilization effect on the energy of the acceptor orbital, but the HS state is also a signature of a weak equatorial ligand field. The weak equatorial ligands that induce the HS state by generating a small splitting between the $d_{x^2-y^2}$ and d_{xy} orbitals, so they become occupied with one up-spin electron each, and also push less electron charge onto the metal than strong ligands do. The lower electronic charge density, i.e., higher positive charge, implies a relative lowering of the orbital energies, including the acceptor orbital. Stronger ligand fields, such as the nitrogen lone-pair donors in the porphyrinic ring of P450 and many

Received: April 12, 2011

Published: December 19, 2011

biomimetic complexes, can also shift the emphasis more toward π^* as the preferred acceptor orbital, as is, for instance, well-known from the extensive work on the P450 systems.^{1–4,6a,c,7}

The prototype dinuclear iron oxo system for C–H bond hydroxylation is the so-called iron oxo diamond core in the active center of the methane monooxygenase (MMO) enzyme in methanotrophs, bacteria that consume methane. They live at the boundary of aerobic and anaerobic environments, having access to both methane and dioxygen and selectively oxidizing methane to methanol¹¹ using dioxygen as the oxidant.^{12,13} Methanotrophs thus play an important role in the global carbon cycle by limiting the amount of methane that reaches the atmosphere.¹⁴ The first step of methane metabolism (oxidation of methane to methanol) has attracted considerable attention because it involves the selective oxidation of the very stable C–H bond in methane under ambient conditions. This is still a challenge for a synthetic catalyst.^{15–17}

The enzyme MMO exists in two different forms, namely, cytoplasmic soluble MMO (sMMO) and membrane-bound particulate MMO (pMMO).^{18,19} The former contains a diiron active site, while it is hypothesized that for the latter copper clusters serve as the reactive center during hydrolysis of methane.²⁰ Detailed characterization of pMMO has been limited because of its instability and difficulty in isolation and purification.^{21–23} sMMO, on the other hand, has attracted considerable attention. It is relatively stable and easy to purify, and although methane oxygenases from different bacteria have somewhat different properties, some are very nonspecific oxygenases, acting on a broad range of substrates. sMMO is a complex enzyme and contains three protein components: hydroxylase (MMOH), B component (MMOB), and reductase (MMOR).^{24–27} Oxidation of methane is catalyzed by the hydroxylase (MMOH) component, electrons for this reaction are provided by the reductase (MMOR) protein, and MMOB plays regulatory roles. The carboxylate-bridged diiron center, located at the α subunit of the hydroxylase protein (MMOH), effects the oxidation of methane using dioxygen. A wide variety of experimental techniques were employed for the structural characterization of the diiron center on MMOH; details can be found elsewhere.^{20–28}

The chemically reduced MMOH (MMOH_{red}) reacts with dioxygen to produce hydroxylated products and MMOH_{ox}.²⁴ A peroxy intermediate (MMOH_{peroxy}) has been identified during this step, for which a configuration of two HS iron(III) centers having similar coordination geometries has been proposed based on Mössbauer spectral analysis.^{29,30} In the presence of the protein matrix surrounding the diiron center, MMOH_{peroxy} relaxes to a high-valent oxo intermediate, MMOH_Q.³¹ Unlike MMOH_{peroxy}, the decay rate of MMOH_Q increases in the presence of hydrocarbon, leading to the obvious conclusion that the active oxygen intermediate for hydrolysis of methane is MMOH_Q.^{29,31} The structural information of MMOH_Q has been elucidated using extended X-ray absorption fine structure spectral data: a very short Fe–Fe distance of 2.46 Å has been reported, together with one short (1.77 Å) and one long (2.0 Å) Fe–O bond.³² The iron atoms in intermediate Q are bridged by two oxo ligands and one bidentate glutamate ligand. Each iron atom has an additional glutamate ligand and a histidine residue attached in the terminal position. Water is also expected to be present in the first coordination sphere. In order to explain the short Fe–Fe distance in MMOH_Q, an additional carboxylate bridge was also introduced.²⁰ The exact structural data for the intermediate Q is unknown, and therefore different

computational models have been suggested in the past to study the mechanism of methane hydroxylation by MMOH_Q. Four different model systems are available in the literature, namely, the Yoshizawa model,³³ the Morokuma–Basch model,³⁴ the Siegbahn model,¹⁰ and the Friesner–Lippard model.^{28–35} These models differ in their size, spin state, charge, and iron coordination number. All theoretical studies indicated that hydrogen abstraction from methane by the bridging μ -oxo ligand is the rate-determining step for hydroxylation of methane.

In the present contribution, we will compare the electronic structure of compound Q with that of the mononuclear FeO²⁺ moiety. The *geometric* structure of the [Fe^{IV}(μ -O)₂] diamond core has led to the suggestion that maybe it can be considered as a dimer of two Fe^{IV}O²⁺ units.³² May this actually be the correct way to view the *electronic* structure? The electronic structure and, in particular, the nature of the acceptor orbital and the mechanism of the hydrogen-abstraction step are the subject of our analysis. On the basis of the present density functional theory (DFT) computations, we, in fact, were able to establish a strong electronic analogy between FeO(H₂O)₅²⁺ and the reactive intermediate, MMOH_Q. However, equally important, there is a significant difference in the reaction mechanism and reaction barrier in the mononuclear and dinuclear iron oxo systems. The first is a prototype catalytic reaction governed by *activation strain*: the activation energy comes from the strain energy of the lengthening of the strong C–H bond toward the transition state (TS). The latter has a reaction barrier that is mostly determined by steric hindrance effects, leading to a significantly higher barrier. We will consider the possible consequences of this difference between MMO and the mononuclear Fe^{IV}O²⁺ catalysts for selectivity of the catalytic reaction for methane oxidation.

2. COMPUTATIONAL METHODOLOGIES

Our computations involve DFT using the OPBE functional³⁶ implemented in the ADF (Amsterdam Density Functional) program package.³⁷ The MOs are expanded in terms of Slater-type orbitals (STO), and all electrons are included in the calculation. A quadruple- ζ basis set with four sets of polarization functions (QZ4P) is used for iron, and a triple- ζ basis set with two sets of polarization functions (TZ2P) is used for other atoms, as available in the ADF library of standard basis sets. Additionally, the calculations were corrected for relativistic effects using the zero-order regular approximation (ZORA) approach.³⁸ The OPBE functional has been chosen, as in our previous work,^{7,9a,39} because this functional has been shown in the literature to be most suitable to describe the close-lying spin states in biologically relevant iron and other transition-metal complexes,^{40a–c} whereas the B3LYP functional has been documented to be problematic.^{40b} The OPBE functional is a combination of the OPTX exchange functional^{41a} and the Perdew–Burke–Ernzerhof (PBE) correlation functional.^{41b} OPTX has also been used in combination with the Lee–Yang–Parr correlation functional^{41c} to form the OLYP functional. Favorable reports have also been given that OPTX-based functionals like OPBE and OLYP perform very well for other properties as well, like bond energies and geometries,^{40a,d–f} including specifically the MMOH_Q system.^{40f} Although it has become clear there are problems with the B3LYP functional for the spin states of iron complexes,^{40b} this functional has mostly been used in previous work on MMOH_Q. We have therefore also computed the energy profile for the C–H dissociation using the B3LYP functional in conjunction with various Gaussian basis sets ranging from small (SVP) to large (def2-QZVPP/TZVPP for iron/other atoms). These computations are performed with the *Turbomole*⁴² program package and are reported in the respective sections.

3. RESULTS AND DISCUSSION

a. Electronic Structure of $\text{FeO}(\text{H}_2\text{O})_5^{2+}$. It is illustrative to start from the electronic structure of $\text{FeO}(\text{H}_2\text{O})_5^{2+}$, which is in its quintet ground state. The valence orbital structure of this complex is given in Figure 1. The basic bonding pattern of Fe–

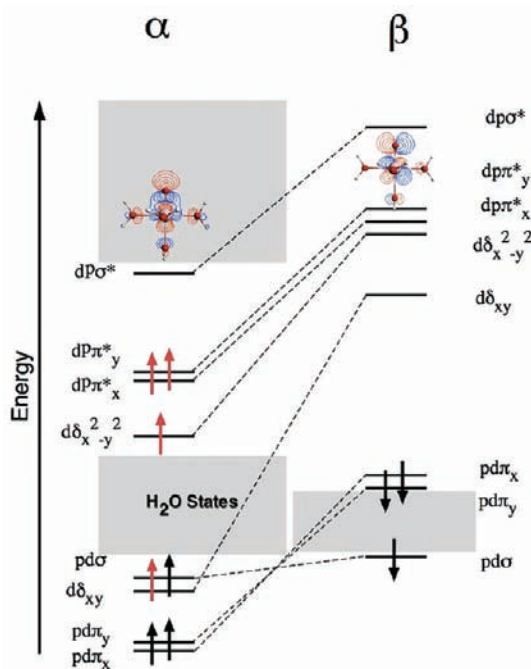


Figure 1. Valence orbital level diagram for the complex $\text{FeO}(\text{H}_2\text{O})_5^{2+}$ in the quintet state. In order to simplify the diagram, only Fe–O states are illustrated. H_2O states are represented using gray boxes and unpaired electrons with red arrows.

O is similar to that of dioxygen:¹ there are three occupied bonding orbitals ($\text{pd}\sigma$, $\text{pd}\pi_x$, and $\text{pd}\pi_y$; see the black up and down arrows in the α - and β -spin orbitals in Figure 1), and there are two unpaired electrons (red arrows) in the antibonding $\text{dp}\pi_x^*$ and $\text{dp}\pi_y^*$. We denote the low-lying bonding combinations of ligand with metal levels (in this case, O 2p and Fe 3d orbitals, respectively), which are nominally “ligand levels” as $\text{pd}\sigma$ and $\text{pd}\pi$ (leading p contribution); the higher-lying antibonding levels, which are nominally “d levels”, are denoted as $\text{dp}\sigma^*$ and $\text{dp}\pi^*$ (leading d contribution). In cases of very short and strong bonds, such as here between iron and oxygen, the actual O 2p and Fe 3d character percentages of these levels may not be predominantly ligand in the lower and metal in the upper levels, but they will tend to equalize and could even reverse. The difference of the FeO^{2+} electronic structure with the basic O_2 -type bonding scheme is in the presence of the two nonbonding 3d orbitals on iron of δ symmetry with respect to the Fe–O axis, the $d_{x^2-y^2}$ and d_{xy} orbitals. They contain the remaining two unpaired electrons (all unpaired electrons are denoted with red arrows), which, added to the two unpaired electrons in the π^* levels, lead to the quintet state. If, however, the equatorial field is very strong, it destabilizes $d_{x^2-y^2}$ so much that the HS configuration $(d_{xy}\alpha)^1(d_{x^2-y^2}\alpha)^1(\text{dp}\pi_x^*\alpha)^1(\text{dp}\pi_y^*\alpha)^1$ reverts to the spin-paired low-spin configuration $(d_{xy})^2(\text{dp}\pi_x^*\alpha)^1(\text{dp}\pi_y^*\alpha)^1(d_{x^2-y^2})^0$. In that case, the triplet state for the two remaining unpaired electrons $(\text{dp}\pi_x^*\alpha)^1(\text{dp}\pi_y^*\alpha)^1$ results. The low-lying vacant $\text{dp}\sigma^*\alpha$ orbital, which is antibonding between the Fe d_z and O

p_z orbitals, is also displayed in the level diagram, as is the LUMO, β -spin $d\delta_{xy}$. The very high reactivity of the $\text{FeO}(\text{H}_2\text{O})_5^{2+}$ complex is attributed to the presence of the lowest-lying acceptor orbital, $\text{dp}\sigma^*\alpha$.^{7,43} This orbital has a relatively large lobe centered on the oxygen atom of the FeO^{2+} unit, facilitating the electron transfer from the occupied C–H bonding orbital of methane. The electronic structure of FeO^{2+} complexes depends not only on the equatorial ligands but also on the trans axial ligand. Strong ligands such as NH_3 when axially substituted will push the $\text{dp}\sigma^*$ orbital up considerably, reducing the electrophilicity of the complex, and vice versa for weak (or absent) axial ligands.⁹ Previous computation on first-row transition-metal oxide dications demonstrated that the σ^* -controlled reactions with a linear approach (in the direction of the Fe–O axis, $\angle\text{H–O–Fe} \approx 180^\circ$) present lower activation barriers than the π^* -controlled ones (with a bent approach, $\angle\text{H–O–Fe}$ between 180° and 90°) because of the steric interaction in the latter case with the equatorial ligands.^{8,43} It is generally accepted that the oxidative action of $\text{FeO}(\text{H}_2\text{O})_5^{2+}$ directly correlates to the electrophilicity of the lowest-lying acceptor orbital, and such an acid–base mechanism can be applied to many biological systems composed of $\text{Fe}^{\text{IV}}(\text{O})_2^{2+}$ units.

b. Electronic Structure of the $[\text{Fe}^{\text{IV}}(\mu\text{-O})_2]$ Diamond Core in a Model Complex for MMOH_Q . We now turn to the relation of the electronic structure of $\text{FeO}(\text{H}_2\text{O})_5^{2+}$ and that of our model complex for MMOH_Q . Out of the four different model complexes proposed for compound Q, we have used the larger Morokuma–Basch model³⁴ in our present analysis (see Figure 2), with two imidazoles representing the

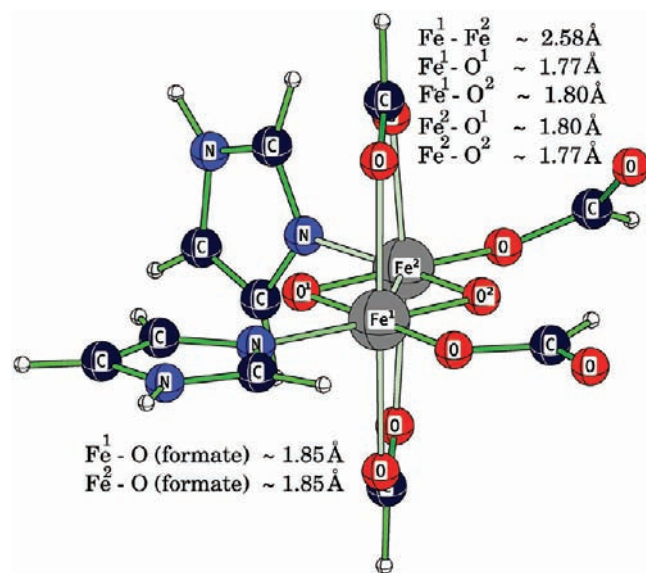


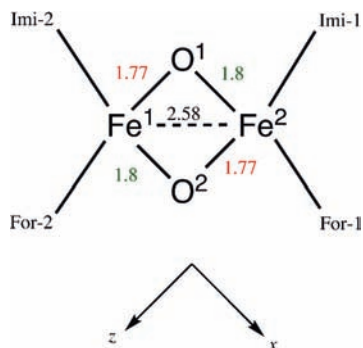
Figure 2. Optimized geometry of the model complex of methane monooxygenase (MMOH_Q) at the OPBE level (^9A state).

histidines, two bridging formates representing the bridging glutamate residues, and two formate ligands representing terminally coordinating glutamate residues (see ref 28 for a comparison of the various models). This model has been largely agreed upon, although we note that Friesner et al. have argued that one of the carboxylate bridges should be replaced by a terminal carboxylate ligand at one iron and a H_2O ligand at the other iron, with the bridge being formed by a more flexible hydrogen bond between these ligands. However, such changes in the model complex will leave the qualitative features of the

inherent electronic structure of the diiron core largely unperturbed. Each iron atom in this model complex is in an octahedral environment, coordinatively saturated with six ligands. The optimized geometry of this model complex at the OPBE level is given in Figure 2. Note that the two imidazole rings representing histidine residues are *cis* to each other. In the present contribution, we consider the O-side reaction by this model complex due to the fact that the N-side reaction will be sterically more hindered by the bulky histidine residues in the real enzyme.^{34b,c} The net charge of the molecule is set to zero, and a HS ⁹A electronic state is considered for the present analysis. This means that we are considering a HS configuration of ferromagnetically coupled $S = 2$ iron centers. We have also performed calculations with the OPBE functional for the antiferromagnetically coupled $S = 2$ centers ("broken symmetry" calculations with spins up on one side and down on the other side), at both the B3LYP- and OPBE-optimized geometry. In both cases, we find the broken-symmetry state with the OPBE functional to be lower than the HS state, but not by much (a few kilocalories per mole). More importantly, we find the frontier orbitals to give basically the same level pattern and have the same shapes as in the HS state (see the discussion below). The exchange coupling between the two iron centers is much less important (and energetically a much smaller effect) than the chemical reactivity (bond breaking and forming) that we are studying here. We refer to ref 44 for a discussion of the very limited effect of antiferromagnetic versus ferromagnetic coupling in a dinuclear iron complex during chemical transformations, such as, in that study, the bond breaking of dioxygen to form two FeO^{2+} reactive centers. Given these findings and given the fact that the HS state is computationally much more expedient, which is important in view of the many calculations needed to trace a complete reaction path (see below), we have chosen to carry out the analysis for the HS state.

The geometrical parameters for the diiron core of this model complex are given in Scheme 1. A very short Fe–Fe bond

Scheme 1. Geometrical Parameters of the Fe–O–O–Fe Diamond Core of MMOH_Q at the OPBE level^a



^aThe bond lengths are given in angstrom units. The local axis frame chosen for MO analysis is also depicted in the scheme.

length of magnitude 2.58 Å is in agreement with the experimental value of 2.46 Å. The available experimental data suggest two distinct FeO^{2+} units with two long (2 Å) and two short (1.77 Å) Fe–O bonds. Our OPBE computations, however, predict FeO^{2+} bond lengths of rather similar magnitude, 1.77 and 1.80 Å. It should be noted that the predicted FeO^{2+} bond lengths depend also on the choice of the

functional; geometrical parameters for the diiron core of MMOH_Q computed using different DFT functionals are given in Table 1. It can be observed that the functionals BP86, OLYP,

Table 1. Geometrical Parameters of the Diiron Core of the Model System for MMOH_Q at Different Levels^a

method	Fe ¹ –O ¹	Fe ² –O ²	Fe ¹ –Fe ²
BP86	1.78	1.82	2.6
OLYP	1.78	1.82	2.6
BLYP	1.79	1.84	2.63
OPBE	1.77	1.80	2.58
B3LYP	1.70	2.02	2.69
experimental	1.77	2.0	2.46

^aBond lengths are given in angstrom units.

BLYP, and OPBE all give a very accurate Fe¹–O¹ bond length, 1.77–1.79 Å. The second Fe–O bond length, Fe²–O², is distinctly longer but is, with 1.80–1.84 Å, too short compared to experiment. Only the B3LYP functional has this second Fe–O bond (2.02 Å) close to experiment, but it has the first Fe–O bond too short (1.70 Å). Despite the geometric distinction between the FeO^{2+} moieties not being very pronounced with the pure (nonhybrid) density functionals, we can still qualitatively analyze the electronic structure of the diiron center and compare it to that of $\text{FeO}(\text{H}_2\text{O})_5^{2+}$.

The valence MO level diagram for the model complex of MMOH_Q in its ⁹A state is represented in Figure 3. In an attempt to simplify the level diagram, only MOs of the two FeO^{2+} fragments are represented; the manifolds of the ligand orbitals are indicated using gray boxes. Labels 1 and 2 refer to the two FeO^{2+} fragments, as indicated in Figure 2. The oxo group at the side of the terminal formate ligands together with the iron atom to which the imidazole ring that is perpendicular to the Fe–O–Fe–O plane is trans axially coordinated, is denoted as fragment 2, $[\text{Fe}^2\text{O}^{2+}]^{2+}$. The other FeO^{2+} fragment, referred to hereafter as Fe¹O¹ (fragment 1), has a trans axial formate ligand. There is a clear correlation between the MMOH_Q and $\text{FeO}(\text{H}_2\text{O})_5^{2+}$ MOs. The σ and π bonds for both fragments 1 and 2 appear as the six lowest occupied orbitals (of course, in both the α - and β -spin manifolds because the orbitals are doubly occupied). Sometimes these bonding orbitals on fragments 1 and 2 mix, forming + and – combinations, such as $(\text{pd}\sigma(1)+\text{pd}\sigma(2))\beta$, and sometimes they are localized on one or the other fragment, such as $\text{pd}\sigma(1)\alpha$ and $\text{pd}\sigma(2)\alpha$ (the numbers given in parentheses are used to distinguish between the two FeO^{2+} fragments). The $S = 2$ iron centers are represented by the eight unpaired α -spin electrons, four in the antibonding π^* MOs ($\text{dp}\pi^*_x$ and $\text{dp}\pi^*_y$), and four in the δ ($\text{d}\delta_{xy}$ and $\text{d}\delta_{x^2-y^2}$) orbitals; see the red arrows in Figure 3. This is just a doubling of the situation that we observed in $\text{FeO}(\text{H}_2\text{O})_5^{2+}$. The most important acceptor orbital will prove to be, just as in all other FeO^{2+} systems, the lowest-lying α -spin unoccupied orbital, the σ^* orbital $\text{dp}\sigma^*\alpha(2)$. It is displayed in Figure 3, as is $\text{dp}\sigma^*(2)$ (see the left green arrows). The σ^* orbitals are pushed up in energy by the strong imidazole ligands, axially coordinated to the Fe^2O^{2+} unit and equatorially coordinated to Fe¹O¹.⁹ The $\text{dp}\sigma^*\alpha(2)$ orbital has the largest lobe on the oxygen atom of the $[\text{Fe}^2\text{O}^{2+}]^{2+}$ unit (fragment 2) and is oriented toward the "open" site adjacent to the terminal formate ligands (see Figure 4). As is visible in the orbital plot of Figure 4, it also has some amplitude on O¹, which arises from the antibonding of an O¹ p_x lone pair with the $\text{d}_{z^2}(\text{Fe}^2)$. It

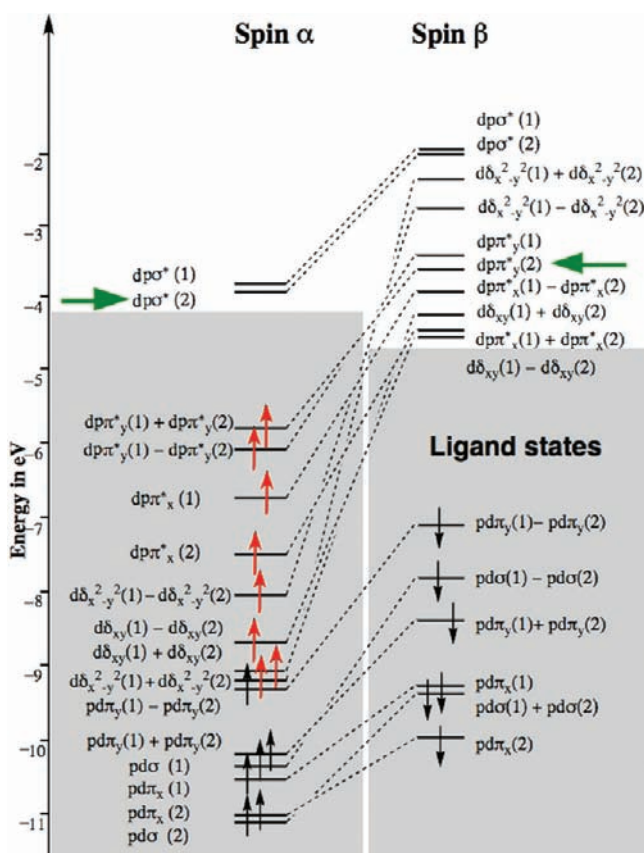


Figure 3. Valence orbital level diagram for the model complex of MMOH_Q (compound Q) in the ⁹A state. In order to simplify the diagram, only Fe–O states are illustrated. Ligand states are represented using gray boxes and unpaired electrons with red arrows. Horizontal arrows point at the important acceptor orbitals.

shows that the O¹ of the Fe¹O¹ oxidoiron group is acting as a ligand to Fe² (as does, of course, O² to Fe¹). $dp\sigma^*\alpha(1)$ has the largest amplitude on O¹ but also some amplitude on O². The large amplitude on O² makes $dp\sigma^*\alpha(2)$ an excellent acceptor orbital for the incoming methane, but we will see that the relatively small amplitude on O² of $dp\sigma^*\alpha(1)$ is not enough to make it an effective acceptor orbital for methane. In the β -spin manifold, the LUMO of MMOH_Q is the β -spin $d\delta_{xy}(1) - d\delta_{xy}(2)$ MO. This is not an important acceptor orbital, being shielded by the ligands. The LUMO of MMOH_Q that can act as an acceptor orbital is the β -spin $dp\pi^*_x(1) + dp\pi^*_x(2)$ orbital (not shown in Figure 4). There is a strong mixing between the two $dp\pi^*_x$ -type MOs of fragments 1 and 2. This orbital has a lobe in the Fe–O–O–Fe plane, but as we will see, it is again not a good acceptor orbital. The counterpart of the + combination, the – combination ($dp\pi^*_x(1) - dp\pi^*_x(2)$) β , is energetically ~ 0.4 eV above the former and has, because of a nodal surface through the O₂, almost no resulting amplitude in the ground plane and therefore no acceptor function. We finally have the $dp\pi^*_y\beta$ orbitals (see right green arrow) as possible acceptor orbitals, depicted in Figure 4. They are oriented perpendicular to the Fe–O–Fe–O plane. $dp\pi^*_y\beta(2)$ and $dp\pi^*_y\beta(1)$ do not mix. $dp\pi^*_y\beta(1)$ has very little amplitude at O₂, but $dp\pi^*_y\beta(2)$ has a large amplitude on O₂ (see Figure 4) and can act as an acceptor orbital if the methane does not approach with the C–H bond in the Fe–O–O–Fe plane, but tilted out of that plane so as to build up overlap with one of the lobes of $dp\pi^*_y\beta(2)$.

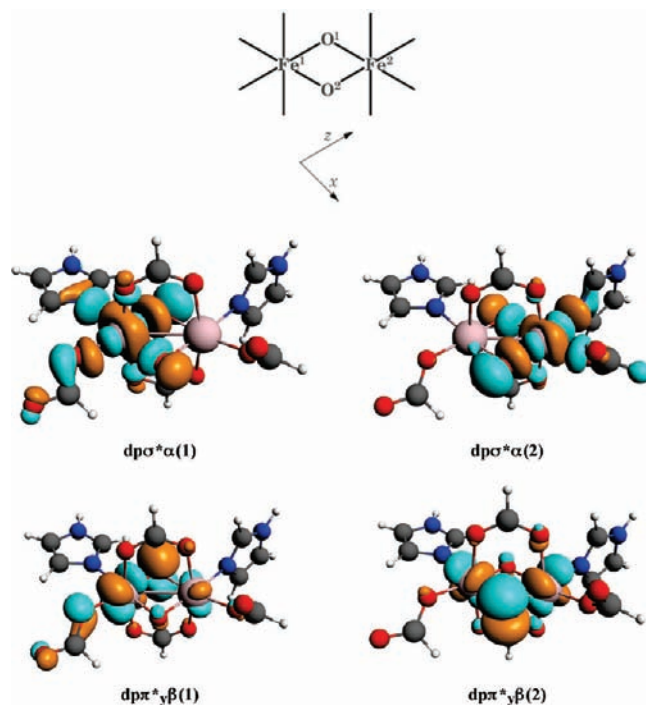


Figure 4. Shapes of important frontier MOs for the model complex of MMOH_Q at the OPBE level. The fragment on which the orbitals are mostly localized is indicated in parentheses.

c. Fragment Analysis of the Electronic Structure of the MMOH_Q Model Complex. The picture of the electronic structure of MMOH_Q that emerges from the character and the energies of the MOs can be analyzed further using the fragment orbital analysis as it is implemented in the ADF package.³⁷ The complex after full geometry optimization is divided into eight fragments: two FeO²⁺ fragments, two imidazole fragments, and four formate fragments. MOs are generated for each of these fragments, and the total electronic structure is then recomputed based on the fragment orbitals.⁴⁵ It is then possible to determine the contributions of the fragment orbitals to the MOs of the complex. The fragment orbital analysis can only be performed with a set of spin-restricted fragment orbitals. Therefore, all fragment MOs are generated with spin-restricted fragment calculations.

The nature of the MMOH_Q orbitals discussed above is substantiated by analysis of the gross populations of the relevant fragment orbitals, as given in Table 2. It is clear from the table that the lower-lying α -spin $p\delta\alpha$ and the (out-of-plane) $pd\pi_y\alpha$ and $dp\pi^*_y\alpha$ orbitals of FeO²⁺ remain practically occupied. Only $pd\pi_x\alpha$ and $dp\pi^*_x\alpha$ (in the Fe–O–O–Fe plane) lose electronic charge to the other FeO group, in agreement with the O¹ character mixed into $dp\sigma^*\alpha(2)$ and the O² character mixed into $dp\sigma^*\alpha(1)$ that we observed in Figure 4. The donation of charge from the $pd\pi_x\alpha$ and $dp\pi^*_x\alpha$ orbitals is into $dp\sigma^*\alpha$, which acquires a substantial electron population (ca. 0.5 electrons). For the β -spin orbitals, there is more charge rearrangement. There is a series of empty $d\beta$ orbitals on the iron atoms (see Figure 1), which all pick up charge (the in-plane $d\delta_{x^2-y^2}\beta$ and $dp\pi^*_x\beta$ the most) from the lower-lying occupied $pd\pi_y\beta$, $pd\pi_x\beta$, and $pd\sigma\beta$. All of these charge donations represent the fact that one FeO (or rather an oxo group) is a ligand to the other FeO group and vice versa. The occupied orbitals of one FeO group can donate to the empty orbitals of

Table 2. Fragment Analysis of the Model Complex of MMOH_Q at Its ⁹A State^a

type of orbital	spin α		spin β	
	Fe ¹ O ¹	Fe ² O ²	Fe ¹ O ¹	Fe ² O ²
pd σ	0.99	0.99	0.89	0.90
pd π_x	0.93	0.93	0.66	0.64
pd π_y	0.99	0.99	0.72	0.72
d $d_{x^2-y^2}$	0.93	0.87	0.31	0.31
d d_{xy}	0.99	0.98	0.18	0.22
dp π_x^*	0.87	0.87	0.32	0.31
dp π_y^*	0.97	0.98	0.24	0.17
dp σ^*	0.45	0.53	0.22	0.19

^aThe gross populations (summation over their populations in all of the occupied MMOH_Q MOs) for the relevant FeO fragment MOs are given above. The entries in columns Fe¹O¹ and Fe²O² respectively refer to populations of the orbitals of the indicated type (e.g., pd σ), one on Fe¹O¹ (pd σ (1)) and one on Fe²O² (pd σ (2)).

the neighbor FeO, i.e., to the whole set of unoccupied β -spin orbitals in the level diagram represented in Figure 3. It should be kept in mind that the orbitals for which the populations are given in Table 2 are orbitals of the FeO²⁺ fragment; they are not the orbitals of the complete MMOH_Q of the same name, that we discussed in connection with Figures 3 and 4. The unoccupied FeO²⁺ orbitals can also receive charge coming from the ligands imidazole and formate. It can be seen from Table 2 that the originally empty α -spin dp σ^* orbital receives considerably more electrons than are coming from the adjacent FeO. It clearly receives electrons donated by the imidazole and formate ligands. This is a result of the “pushing up” of dp σ^* by the nitrogen- and oxygen-donor lone pairs of these ligands. In order to verify this, we have also listed, in Table 3, gross

Table 3. Fragment Analysis of the Model Complex of MMOH_Q at ⁹A State^a

orbital	spin α		spin β	
	formate 1	formate 2	formate 1	formate 2
HOMO	0.84	0.82	0.87	0.87
HOMO-1	0.99	0.99	0.97	0.94
HOMO-2	0.98	0.98	0.91	0.90
orbital	spin α		spin β	
	imidazole 1	imidazole 2	imidazole 1	imidazole 2
HOMO	1.00	1.00	1.00	1.00
HOMO-1	0.89	0.89	0.91	0.91
HOMO-2	1.01	1.00	1.00	0.99
orbital	spin α		spin β	
	bridge 1	bridge 2	bridge 1	bridge 2
HOMO	0.97	0.97	0.85	0.85
HOMO-1	0.98	0.98	0.88	0.88
HOMO-2	0.99	0.99	0.95	0.95

^aThe gross populations (summation over all occupied MOs) of relevant ligand orbitals are given (formate 1 and formate 2 in the Fe–O–O–Fe plane and bridge 1 and bridge 2 are the formate bridges).

populations of relevant ligand fragment orbitals. It is evident that there is a considerable amount of charge transfer from the HOMO-1 orbitals of the imidazoles and the highest occupied molecular orbitals (HOMOs) of the formate ligands lying in the Fe–O–Fe–O plane. These are the lone-pair donor orbitals having large lobes centered on either the nitrogen or oxygen

atoms with which they are directly coordinated to an FeO²⁺ moiety. For the sake of comparison, we have also presented results from the calculation on MMOH_Q using atomic fragments (cf. Table 4). It is clear from the gross electron

Table 4. Fragment Analysis of the Model Complex of MMOH_Q Using Atomic Fragments^a

	spin α		spin β	
	Fe ¹	Fe ²	Fe ¹	Fe ²
3d $_z^2$	0.64	0.71	0.37	0.35
3d $_{x^2-y^2}$	0.92	0.85	0.31	0.32
3d $_y$	0.99	0.99	0.20	0.23
3d $_{xz}$	0.98	0.98	0.22	0.22
3d $_{yz}$	0.99	0.99	0.26	0.24

^aThe gross populations of relevant atomic orbitals (summation over all MOs, multiplied by occupation) are given above.

population that the α -spin d $_{xy}$, d $_{yz}$, d $_{xz}$, and d $_{x^2-y^2}$ orbitals are completely occupied, in agreement with a formal HS d⁴ electron configuration of iron. The α -spin d $_z^2$ orbital has considerable population, owing to its participation in the occupied Fe–O pd σ bonding orbital (although one typically classifies this as a “ligand” (O 2p) orbital). The empty acceptor orbital dp σ^* is nominally the “d $_z$ ” orbital but is certainly not a pure d $_z^2$, having much O 2p $_z$ character. The β -spin Fe 3d orbitals show the charge accumulating as a consequence of donation by the ligands.

In summary, this analysis shows that the dinuclear system can be considered as two FeO groups, each one coordinated by the imidazole and formate ligands and by (the oxo of) the other FeO group.

d. Reaction with CH₄: Comparison between Mononuclear and Dinuclear Iron Oxo Systems. We next study the reaction with CH₄. Of the two oxo groups, the one that is at the side of the terminal formate ligands (O²; see Figure 5) is responsible for the catalytic activity of MMOH_Q. The other FeO²⁺ fragment, referred to hereafter as Fe¹O¹ (fragment 1), is not expected to take part in methane hydroxylation because of the large steric hindrance around O¹ by the bulky histidine residues in the real enzyme. Initially, a very weakly bound reactant complex is formed, with a long O²–C distance of 4.86 Å and the methane tilted ca. 45° out of the Fe–O–O–Fe plane; see Figure 5a. In this complex, the hydrogen that will be abstracted is not yet oriented toward the oxygen. Along the reaction path, the methane turns and the C–H bond lengthens and starts to interact with O². The optimized geometry of the TS structure for hydrogen abstraction by MMOH_Q is illustrated in Figure 5b. The structure has been obtained with a TS search with the large QZ4P/TZ2P STO basis set and the OPBE functional. The TS has been characterized as having a single imaginary frequency of magnitude of 596 cm⁻¹ which corresponds to the elongation of the C–H bond oriented toward the FeO²⁺ fragment. The magnitudes of the C–H and O–H bond lengths are calculated as 1.44 and 1.10 Å, respectively, and the barrier is 32.4 kcal/mol. It should also be noted that at the TS geometry the C–H bond in methane is making an angle of ~33° with respect to the Fe–O–Fe–O plane. From the shape of the main acceptor orbital, dp σ^* , it can be seen that the approach of CH₄ in the equatorial plane would give optimal overlap but the directional preference would not be strong. Moreover, an out-of-plane configuration can be facilitated by involvement of the dp π_y^* orbitals as

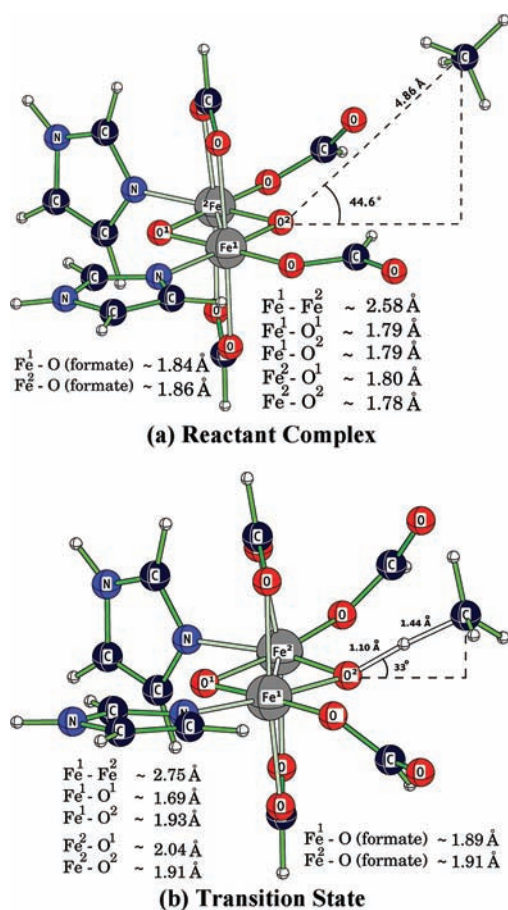


Figure 5. (a) Optimized geometry (OPBE functional) of the reactant complex of the MMOH_Q model with methane. (b) Optimized geometry (OPBE functional) of the TS (TS1) for the hydrogen-abstraction reaction.

acceptor orbitals. In order to find out the nature of the acceptor orbital(s), we have analyzed the TS structure using the fragment MO method. Here, the whole MMOH_Q unit has been considered as one fragment, and the methane molecule is treated as the second unit. The gross populations of relevant fragment MOs are summarized in Table 5 ($\text{dp}\sigma^*$, $\text{dp}\pi^*_{x,y}$ and

Table 5. Fragment Analysis of TS1 for the Model Complex of MMOH_Q^a

orbital	spin α	spin β
$\sigma_{\text{C-H}}$	0.62 (−0.38)	0.88 (−0.12)
$\text{dp}\sigma^*(2)$	0.62 (+0.62)	0.03 (+0.03)
$\text{dp}\pi^*_{x(2)}$	0.99 (−0.01)	0.08 (+0.08)
$\text{dp}\pi^*_{y(2)}$	0.94 (−0.06)	0.10 (+0.10)
$\text{dp}\sigma^*(1)$	0.05 (−0.05)	0.01 (+0.01)
$\text{dp}\pi^*_{x(1)}$	1.00 (0.00)	0.03 (+0.03)
$\text{dp}\pi^*_{y(1)}$	1.00 (0.00)	0.01 (+0.01)

^aThe gross populations of relevant fragment orbitals ($\text{dp}\sigma^*$, $\text{dp}\pi^*_{x,y}$ and $\text{dp}\pi^*_{y}$ of the complex and the $\sigma_{\text{C-H}}$ of the methane) are given above. The difference between the integer gross population in the isolated fragment and the gross population in the TS is given in italic numerals.

$\text{dp}\pi^*_{y}$ of MMOH_Q and $\sigma_{\text{C-H}}$ of methane). The differences between the integer gross populations in the isolated fragment and the gross populations in the TS are given as italic numerals.

It is evident that there is a considerable amount of charge transfer (of magnitude 0.38 electrons) from the $\sigma_{\text{C-H}}\alpha$ bonding MO of methane to the vacant $\text{dp}\sigma^*(2)\alpha$ orbital (centered on fragment 2) of the MMOH_Q complex, which gains in total even 0.62 electronic charge.

There is some gain in the electron population for the $\text{dp}\pi^*_{y}\beta$ orbital (0.10), but this is significantly smaller than that for $\text{dp}\sigma^*(2)\alpha$. This leads us to the conclusion that the important acceptor orbitals that take part in the hydrogen-abstraction step are primarily $\text{dp}\sigma^*(2)\alpha$ and, to a much smaller extent, $\text{dp}\pi^*_{y}\beta(2)$. This is consistent with the fact that the lowest-lying $\text{dp}\pi^*_{y}\beta$ orbital set is energetically 0.48 eV above the $\text{dp}\sigma^*(2)\alpha$ MO, cf. the level diagram of MMOH_Q . The $\text{dp}\pi^*_{y}\beta(2)$ orbital therefore will assist in the bending of the approaching CH_4 out of the equatorial plane, but it does not seem to be the driving force.

e. Origin of the TS Barrier in the Mononuclear and Dinuclear Systems. The bent geometry of the TS for the hydrogen-abstraction step is contrary to the expected in-plane TS for the σ^* -controlled reactions; compare, e.g., the “linear” TS in the prototypical $\text{FeO}(\text{H}_2\text{O})_5^{2+}$.⁸ The barrier is also much higher than the 2.2 kcal/mol OPBE barrier of $\text{FeO}(\text{H}_2\text{O})_5^{2+}$. We therefore compare the hydrogen abstraction in the model MMOH_Q system with the hydrogen abstraction by $\text{FeO}(\text{H}_2\text{O})_5^{2+}$. We note that the 2+ charge on the $\text{FeO}(\text{H}_2\text{O})_5^{2+}$ and the zero charge on the MMOH_Q model is a significant difference. Because however, as we will see, the important difference between the mononuclear and dinuclear systems arises from steric hindrance effects, which are not as sensitive to charge effects, the comparison is still helpful. Figure 6a illustrates the total energy profile for the C–H dissociation (red curve). It is interesting to compare this total energy with the strain energy that builds up in the methane fragment (blue curve) and with the summed strain energy of the methane and $\text{FeO}(\text{H}_2\text{O})_5^{2+}$ fragments (green curve). It should be noted that the bond energy of the C–H bond in methane is ca. 105 kcal/mol, so we show in this figure just the beginning of the bond stretching process. The red curve for the bond breaking in the presence of $\text{FeO}(\text{H}_2\text{O})_5^{2+}$ shows quite strikingly the catalytic action of this species: the increasing interaction with $\text{FeO}(\text{H}_2\text{O})_5^{2+}$ when the C–H bond is stretched, which is mostly $\sigma(\text{C-H})$ to $\sigma^*(\text{FeO}^{2+})$ electron donation, enormously lowers the energy needed to break the bond. The energy profile along the reaction path is generated by optimizing at each C–H bond length all other geometric parameters. This is possible because the C–H bond length is a reasonable approximation of the reaction coordinate in this case. This is the typical picture of a reaction barrier that can be understood in terms of two important contributions: (1) the strain energy required to effect the important geometry change for the reaction—in our case, the C–H bond lengthening; (2) the energy lowering due to interaction between the reactants—this is usually the orbital interaction of occupied and virtual orbitals (orbital control) but can, of course, also have an important or even dominant electrostatic interaction component (charge control).⁴⁶ In the present case, also the $\text{FeO}(\text{H}_2\text{O})_5^{2+}$ fragment distorts to increase the favorable interaction. For more details on the description of TS barriers in terms of activation strain as the main cause for a barrier and orbital interaction as the important lowering mechanism, we refer to ref 46.

For the MMOH_Q case, the C–H stretch coordinate is not a good reaction coordinate in the initial stages of the reaction, as will become apparent below. In order to obtain a more

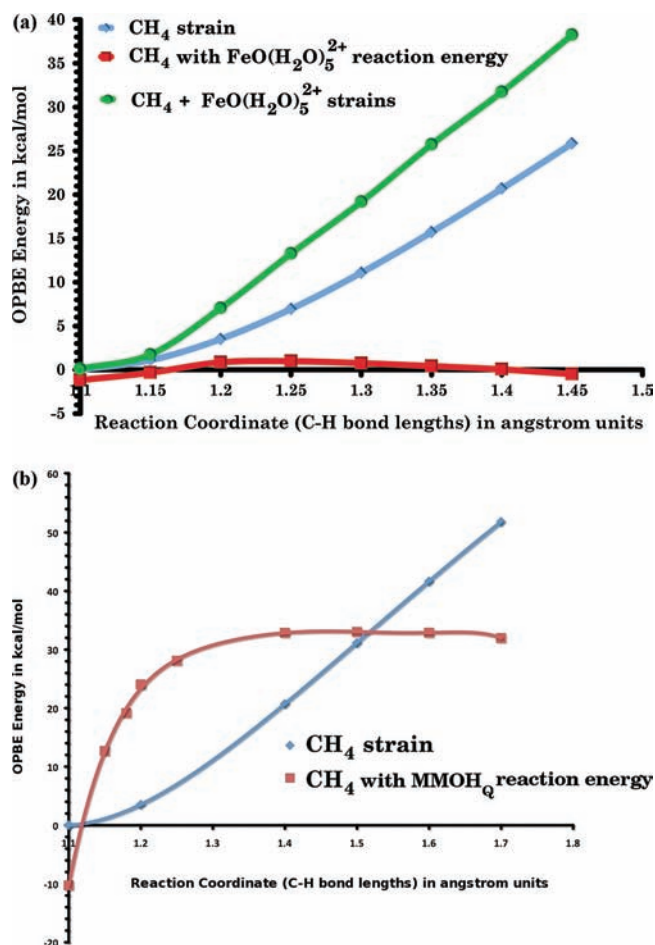


Figure 6. Reaction profiles for C–H dissociation: (a) in the presence of $\text{FeO}(\text{H}_2\text{O})_5^{2+}$ at the OPBE level; (b) in the presence of the model complex MMOH_Q at the OPBE/QZ4P/TZ2P level. The C–H bond dissociation curve for the isolated methane molecule (i.e., the strain energy in the CH_4 fragment) is represented using the blue curve. The sum of the strain energies of the CH_4 and $\text{FeO}(\text{H}_2\text{O})_5^{2+}$ fragments is represented with a green curve in panel a. The zero of the energy scale is always the isolated, geometry-optimized molecules (just CH_4 for the blue curve; the sum of CH_4 and $\text{FeO}(\text{H}_2\text{O})_5^{2+}$ or MMOH_Q systems for the red curves). In all cases, the chosen reaction coordinate is just the C–H bond length.

complete picture of the reaction path, we have calculated a two-dimensional (2D) contour plot of the energy surface by calculating the energy at a large number of O–H and C–H bond lengths, optimizing at each point all of the other geometrical parameters of the system. This provides a 2D cut through the total energy hypersurface. The contour plot of the energy is shown in Figure 7. The system starts at the geometry of the reactant complex at C–H ~ 1.09 Å and O–H bond length 4.86 Å (this point is outside the 2D plot of Figure 7). The barrier at the OPBE level is 32.4 kcal/mol. This is much higher than the 2.2 kcal/mol OPBE barrier for $\text{FeO}(\text{H}_2\text{O})_5^{2+}$. This is an important finding that sets the dinuclear system apart from the mononuclear one, in spite of the electronic similarity that we have observed. We will in the next section give an energy decomposition analysis of the origin of this large difference.

The barrier we find is also considerably higher than the barriers obtained in earlier work on the MMOH_Q model system, which have been estimated from 10–12¹⁰ to 13.3 (22–

23 in a smaller model)³⁴ to 17.9³⁵ kcal/mol. Also, typically an earlier TS was found (at C–H bond length 1.13,¹⁰ 1.246,³⁴ and 1.258 Å³⁵). These results were all obtained with the B3LYP functional, usually with geometry optimization (TS search) in a small basis and recomputation the energies at fixed geometry in a larger basis. We have therefore also performed calculations with the B3LYP functional, using our very large STO basis (QZ4P/TZ2P) with *ADF*, as well as using medium to large Gaussian basis sets (up to def2-QZVPP/TZVPP for iron/other atoms with the *Turbomole* program⁴²). We find with both the large STO and the large Gaussian basis sets that the B3LYP functional yields a substantially lower barrier than OPBE (slightly under 20 kcal/mol). This is still much higher than the barrier in the mononuclear system. We have verified that the energy decomposition to be discussed in the next section, when performed with the B3LYP functional at the B3LYP-optimized TS, yields the same picture as OPBE for the energy terms responsible for the difference between mononuclear and dinuclear systems (see the next section). Concerning the fact that our current B3LYP calculations give a higher barrier than most of the older calculations, we note the following. We have found that the B3LYP calculations are rather sensitive to the basis set used. With the smaller basis sets, a too early TS is found, as a local maximum. When continuing along the reaction coordinate, eventually a second higher maximum is reached. Small and medium basis set calculations may therefore find a TS at an earlier point along the intrinsic reaction coordinate than that obtained with the large basis set calculations. Carrying out an energy calculation with a large basis at this early point will then still yield a too low estimate for the barrier. The large basis set B3LYP calculations did not exhibit this phenomenon. With respect to the difference between the functionals, we note that there is considerable variance over the many functionals that can be used, the basis set, and other aspects such as the choice of pseudopotentials (which have invariably been used in the earlier calculations). We also note that when dispersion corrections using the DFT-D parametrization of Grimme are applied, the barrier lowers by 4–5 kcal/mol, although dispersion energies per se would not be expected to affect the barrier significantly. With the present state of the art in computational technology, it is not possible to establish the precise height of the barrier from calculations alone. However, we are not concerned here with the precise height of the barrier, but we want to analyze why the energy profile of the reaction, depicted in Figure 6b (see discussion below), is so different from that in the mononuclear case. The shape of Figure 6b (much *higher* energy until the TS, and beyond, than the strain energy of methane) is obtained with both OPBE and B3LYP and the various basis sets (large STO, small, intermediate and large Gaussian basis sets) and programs (*ADF* and *Turbomole*).

We note that the automatic OPBE TS search had given the TS at C–H = 1.44 Å and O–H = 1.10 Å. This is somewhat off the TS point one would deduce from the 2D plot (C–H = 1.55 Å; O–H = 1.05 Å). However, we observe that the energy around the TS is very flat, in particular in the C–H coordinate. The OPBE TS point from the automatic geometry search is in between the contour lines –274.98 and –274.97 eV, while the TS point on the 2D plot is at –274.95 eV. The position on the TS “plateau”, i.e., the precise value of, e.g., the C–H distance at the TS energy, is not so meaningful. The distortion of the MMOH_Q fragment, in particular the bending away of the formate groups from the incoming methane, which we

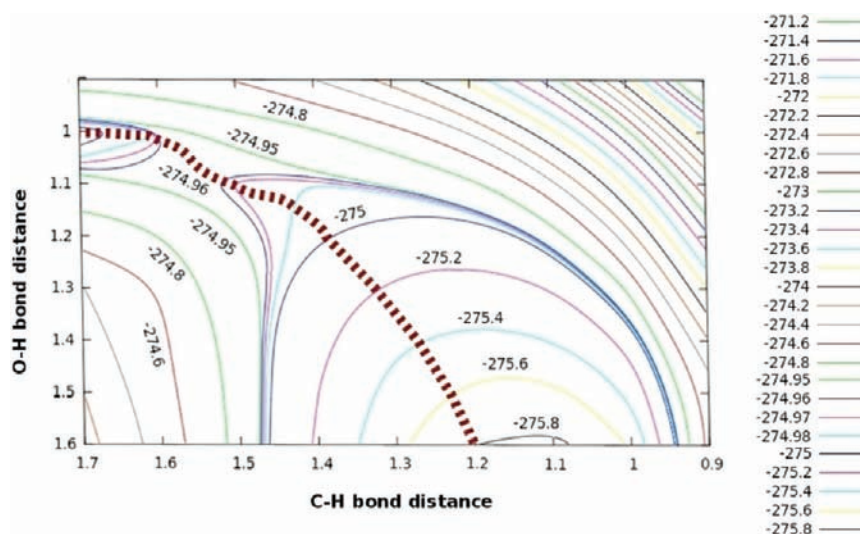


Figure 7. 2D cut through the energy hypersurface for the hydrogen-abstraction reaction by the model complex MMOH_Q . The surface is constructed by calculating the energy at various O–H and C–H distances, optimizing all other geometrical parameters at each point.

observed for the TS geometry of the automatic TS search, is fully intact at the TS point of the 2D contour plot.

In Figure 6b, we give the energy profile as a function of the C–H distance. Because we have the full 2D plot available, we could give the energy profile as a function of the reaction coordinate, with equidistant intervals along the reaction path indicated in Figure 7. However, in order to be comparable to Figure 6a, we use again the C–H distance as the parameter to trace the reaction coordinate. For each C–H value at the horizontal axis of Figure 6b, the corresponding point at the reaction coordinate can be read from Figure 7. Figure 7 substantiates our earlier remark that, in the early stages of the reaction, the C–H distance is not a good reaction coordinate. It is actually almost orthogonal to the intrinsic reaction coordinate: for small C–H change, we travel a long distance along the intrinsic reaction coordinate, and the energy changes strongly, as is observed in Figure 6b. The energy profile in the case of MMOH_Q in Figure 6b shows a strikingly different behavior compared to that of the $\text{FeO}(\text{H}_2\text{O})_5^{2+}$ case of Figure 6a. At C–H distance 1.10 Å, the total energy of the methane + MMOH_Q reactant complex is lower than the sum of the energies of these isolated fragments; the lowering is due to the complexation energy in the initial reactant complex. It is remarkable that, at the TS and for some distance along the reaction coordinate before the TS is reached, the energy is much *higher* than the strain energy of the C–H bond lengthening. Apparently, in this case the TS barrier is *not* caused by activation strain. The energy profile suggests that methane has to overcome a considerable amount of repulsion with the MMOH_Q system before it can profit from the electronic factors that can ease the hydrogen abstraction in the same way as they did in the case of $\text{FeO}(\text{H}_2\text{O})_5^{2+}$. The barrier can obviously be attributed to the steric repulsion that methane experiences from the terminal formate ligands as it approaches the FeO^{2+} unit. Methane has to overcome the Pauli repulsion with, for instance, the HOMO–2 of MMOH_Q , which has a large lobe localized on the noncoordinated oxygen atom of one of the terminal formate ligands. It is indeed notable that the formate ligands have considerably reoriented themselves in the TS (cf. the TS structure in Figure 5b) compared to the free MMOH_Q (Figure 2). There is clearly a bending away from the

methane. The formate attached to Fe^1 goes down with respect to the equatorial plane; the other formate moves up much more than it did in the free complex.

f. Analysis of the TS Barrier. It is of interest to unravel in more detail what are the contributing factors to the barrier. We first carry out analysis for the point along the reaction coordinate where C–H = 1.3 Å, at which point the height of the TS barrier has been practically reached. This analysis will reveal the electronic origin of the height of the barrier, in particular why it is so much higher than the strain energy. The repulsive contributions to the energy are the strain (in both methane and the model MMOH_Q complex) plus the steric repulsion, and the energy-lowering contribution comes from orbital interactions between these two reacting (and deformed) moieties. Figure 6b shows only the strain in methane and the total energy. It does not reveal how much steric repulsion there is and neither the orbital interaction energy. If we go from C–H = 1.3 Å further along the reaction coordinate, the CH_4 strain energy starts to make up an increasing part of the total energy (i.e., of the rise of the energy above the reactant complex). Eventually, at the crossing point between the blue strain energy curve and the red total energy curve, the orbital interaction energy exactly counteracts the steric repulsion and MMOH_Q strain. After the crossing point, the electronic interactions overpower both the steric repulsion and the MMOH_Q strain energy and *lower* the energy below the CH_4 strain value. The activation strain energy is what is usually, in the energy decomposition scheme,⁴⁵ called the “preparation energy”. It is composed of the energies required to distort the interacting systems to their current geometries, which are here the geometries of CH_4 and MMOH_Q at the C–H = 1.3 Å point (the O–H distance is then also ca. 1.3 Å). As mentioned above, for methane the strain comes from the C–H bond lengthening, which amounts to 11.1 kcal/mol C–H = 1.3 Å (see Figure 8 for a diagram of the energies involved). At this point, with still a fairly long O–H distance of 1.3 Å, the strain in the MMOH_Q model only amounts to 1.2 kcal/mol. The activation strain for MMOH_Q comes from a distortion of the total framework, in particular also a bending away of the terminal formate ligands so as to reduce the steric hindrance with the incoming CH_4 . We will consider below a quantification of these geometric

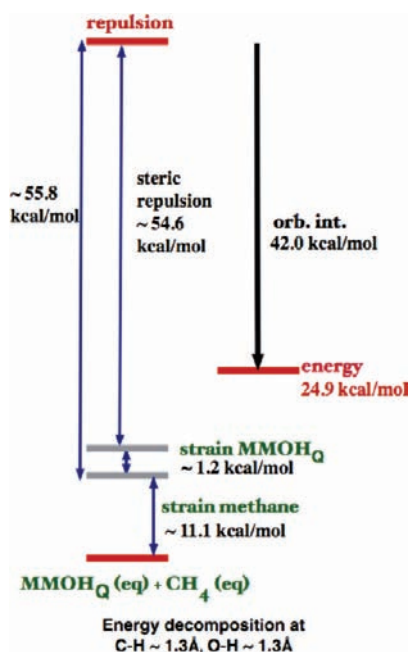


Figure 8. Schematic representation of the strain energies of CH_4 and the MMOH_Q model complex at the point along the reaction coordinate with C–H and O–H bond lengths both 1.3 Å. The steric repulsion between the (strained) CH_4 and MMOH_Q fragments as well as the attractive orbital interaction energy is also shown.

distortions of MMOH_Q . Here we note that the MMOH_Q system cannot distort in such a way that the steric repulsion with the incoming CH_4 is totally avoided. It is actually quite large. We obtain at C–H = 1.3 Å a steric repulsion of 54.6 kcal/mol, which together with the 1.2 kcal/mol strain of the MMOH_Q fragment amounts to a 55.8 kcal/mol energy rise above the activation strain of 11.1 kcal/mol of the C–H bond lengthening (Figure 8). This repulsion is mostly, but not completely, compensated for by a large stabilizing orbital interaction (the C–H donation into the acceptor orbitals of the MMOH_Q) of 42.0 kcal/mol. This analysis demonstrates that large interaction terms are involved apart from the C–H strain energy. The total energy (of 24.9 kcal/mol) is 13.8 kcal/mol higher than the CH_4 strain. This additional 13.8 kcal/mol is actually composed of a much larger steric repulsion, counteracted by a large orbital interaction energy. These large energies are a direct consequence of the fact that CH_4 can only get close to the active oxo oxygen by pushing against the repulsion of the ligand framework. When we do this analysis at the TS at C–H = 1.55 Å, with a shorter CH_4 – MMOH_Q distance (O–H = 1.10 Å), we find that there is even much more steric repulsion, but the orbital interaction then becomes so strong that it outweighs the repulsion and even lowers the total energy a bit below the CH_4 strain energy; see Figure 6b.

Apparently, the formate ligands are important for the steric repulsion. It is of interest to consider the energetics involved in the movement of the formate ligands, both with respect to the strain energies induced by that movement and with respect to the amount of steric repulsion with CH_4 that is relieved or avoided by the “bending away” of the formate ligands. The diagrams of Figure 9 show a quantification of these geometric distortion energies for MMOH_Q at the TS geometry found by the TS search with the OPBE functional, denoted as TS1. The C–H stretch at that point costs 26.9 kcal/mol; see Figure 9b.

The strain in the MMOH_Q framework is 14.8 kcal/mol; see also Figure 9a, which is considerably larger than the strain at C–H = 1.3 Å. One wonders how much of this strain is due to the formates bending away from their orientations in the free MMOH_Q , where they are approximately lying in the equatorial plane, to the positions they have in the TS. Actually, the formates have considerable conformational freedom. This is apparent when we bend the formates to the geometries that they have in the TS, while keeping all other MMOH_Q geometrical parameters constant at the optimized ground-state values. This only gives an energy rise of 4.6 kcal/mol (see Figure 9a), which is only a part of the total strain energy of 14.8 kcal/mol of MMOH_Q to the TS geometry. Alternatively, if we start with the MMOH_Q in the TS1 geometry, and move the formates back to the positions that they had in the free MMOH_Q , again keeping all other geometrical parameters constant, we see to the left in Figure 9a that the energy drops only 1.4 kcal/mol. These small energetic effects underline the conformational freedom of the formates in the MMOH_Q complex. The implication is that if the formates in the equatorial plane of MMOH_Q have considerable steric repulsion with methane approaching in the plane, they can bend away without much energy penalty. The (small) energy involved in the geometrical distortion of the formates, and indeed of the whole MMOH_Q frame, should be “paid back” in the form of more effective interaction (less repulsion, stronger donor–acceptor interaction) with the incoming CH_4 . In the TS, an optimum geometry for minimization of the steric repulsion is found not only by the bending away of the formates but also by the methane moving out of the Fe–O–Fe–O plane (the O–H–C axis makes at TS an angle of 33° with the plane). The bending away of the formates is such that one formate group goes up with respect to the plane and the other one down (but not in a symmetrical way); cf. Figure 5b. In order to obtain a quantitative measure of the energies involved in the various geometric distortions, or rather adaptations, we give in Figure 9b some results of pilot calculations. To the right in Figure 9b are the strain energies of CH_4 and MMOH_Q in TS1 of 26.9 and 14.8 kcal/mol, respectively. Different from the situation at C–H = 1.3 Å, in TS1 the total strain of 41.7 kcal/mol is larger than the total energy (i.e., the TS barrier) of 32.4 kcal/mol. This lowering of the total energy by 9.5 kcal/mol with respect to the strain energy is caused by a huge orbital interaction energy of –121.6 kcal/mol (not shown in the Figure), which outweighs the steric repulsion of +112.1 kcal/mol. To the left in Figure 9b, we see that when we put in TS1 the formate ligands back in the positions that they have in the free model MMOH_Q complex, keeping all of the other geometrical parameters fixed at the TS1 values, including those of the stretched CH_4 , which is now close to the O^2 of the Fe–O–O–Fe diamond core (O–H = 1.10 Å), the energy rises by 31.4 kcal/mol. This is due to increasing steric repulsion of the formates with CH_4 . Equivalently, MMOH_Q can achieve a decrease in the steric repulsion of 32.8 kcal/mol by the flexibility of the formate ligands, for which a “price” of only 1.4 kcal/mol deformation energy of the formates has to be paid. We have also considered whether the methane could approach precisely in the Fe–O–O–Fe plane. As a matter of fact, moving the methane into the plane instead of at 33° above the plane, keeping all other geometrical parameters fixed (including the formates), gives only an energy rise of 1.14 kcal/mol. Obviously, the out-of-plane approach is not a significant geometric feature. We have finally also considered the possibility that the two formates

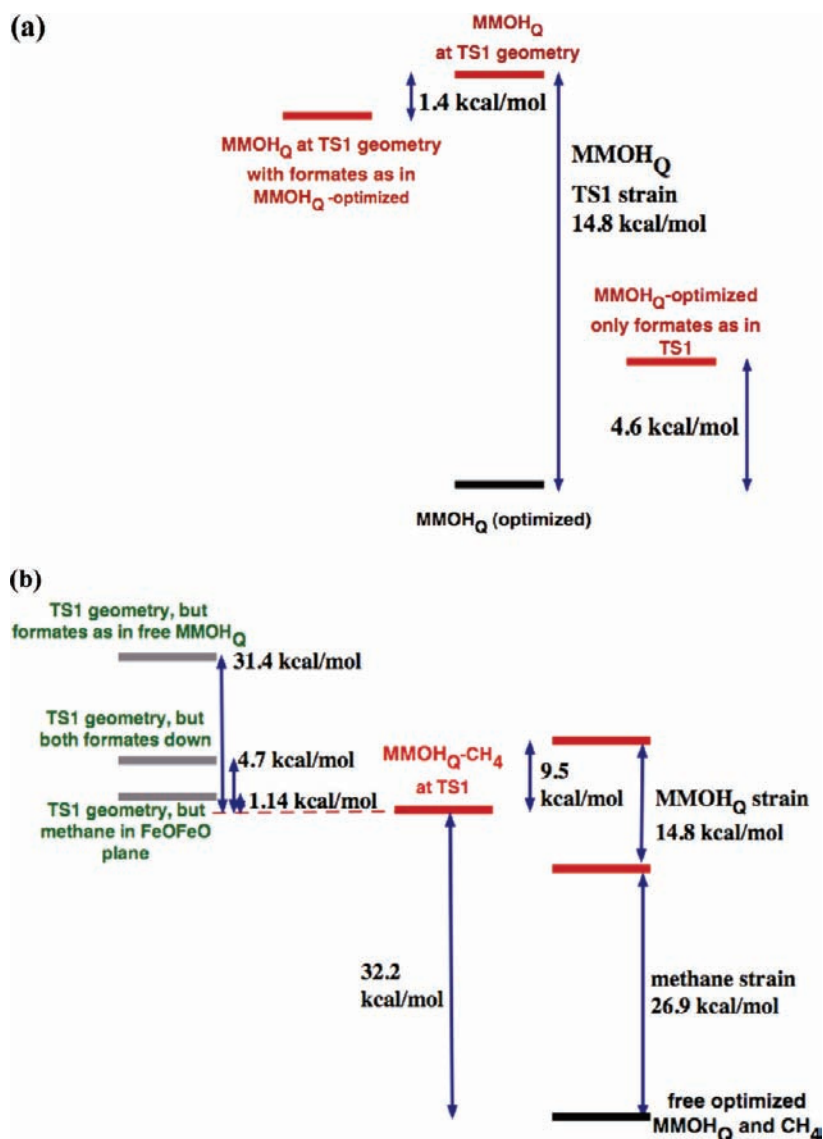


Figure 9. Schematic representation of the energy values associated with geometrical changes of the model complex MMOH_Q. (a) The formates in the isolated MMOH_Q system. To the right: moving the formates to their TS1 positions while keeping the remaining geometrical parameters of the MMOH_Q framework fixed at their ground-state (optimized) values. To the left: moving the formates in the MMOH_Q TS1 geometry back to the ground-state positions. (b) To the right: strain energies at the TS1 geometry. To the left: energetic effects of variation in the positions of the formates and CH₄ in the CH₄-MMOH_Q complex keeping the rest of the MMOH_Q fragment and CH₄ at the TS1 geometry.

would not bend into different directions, but would both go down, while CH₄ stays at the 33° position. That gives an energy rise of only 4.7 kcal/mol above the lowest-energy geometry with one formate up and one down. In conclusion, the formate ligands do have “to get out of the way” (cf. the energy penalty of +31.4 kcal/mol when they do not), but it is not as important how they bend and to what extent CH₄ moves out of the plane.

In conclusion, we find that the Fe–O–O–Fe diamond core is electronically very much analogous to the FeO²⁺ group in mononuclear complexes but has a different reactivity because of the different steric effect of the ligand environment.

4. CONCLUDING REMARKS

We have analyzed the electronic structure of a well-known model complex for compound Q of MMO. Using our fragment MO analysis, we have highlighted the essential electronic similarity of the MMOH_Q complex and the prototype mononuclear FeO²⁺ catalyst FeO(H₂O)₅²⁺. Indeed, compound

Q can not only geometrically but also electronically be considered as a system composed of two coupled FeO²⁺ units, one of which is sufficiently unshielded by ligands to exhibit the typical catalytic activity of FeO²⁺. The hydrogen abstraction is regarded as the rate-determining step for the hydrolysis of methane by MMOH_Q and is associated with an electron transfer from the C–H bonding MO to the low-lying acceptor orbital *dpσ**. This orbital has a relatively large lobe oriented toward the incoming methane and readily accepts electrons from the C–H bonding orbital. We have, however, found an important difference for the hydrogen-abstraction step during the hydrolysis of methane in the dinuclear complex as compared to the FeO(H₂O)₅²⁺ complex. Upon approach to the oxo group in MMOH_Q, methane has also to overcome significant steric repulsion with the terminal formate ligands. This gives the energy profile along the reaction coordinate a very different shape in the case of MMOH_Q. The energy rises considerably above the activation strain of the C–H bond

lengthening because of the steric repulsion that the incoming substrate has to overcome in order to get close enough to the oxo oxygen of the Fe–O–O–Fe diamond core to benefit from the favorable electronic structure of the catalyst. This leads to a significantly higher barrier for the MMOH_Q-catalyzed reaction than with FeO(H₂O)₅²⁺.

We stress that the higher barrier of the methane hydroxylation with our model of MMOH_Q than with the prototype FeO(H₂O)₅²⁺ is most likely not “accidental”. An important problem for the oxidation catalysis of methane is the selectivity: a catalyst that can be used for hydroxylation of the very strong C–H bond of methane will usually also oxidize the methanol product and possibly all further products until the end products of H₂O and CO₂. It is clear that, in principle, methanol is more easily oxidized (to formaldehyde) than methane is to methanol,⁴⁷ which can be easily understood on the basis of the considerably higher orbital energy of the C–H bonding orbital in methanol than in methane because of antibonding of this orbital with the lone pair on oxygen; cf. Figure 1 in ref 48. It is therefore closer to the dσ* acceptor orbital. The electronic factors that make an FeO²⁺ system a good catalyst for the breaking of the very strong C–H bond of CH₄ will make it an even better catalyst for further oxidation of the methanol reaction product. So, in order to make the catalyst selective for methane oxidation, an inhibiting factor has to be introduced, for instance in the form of more steric hindrance for methanol. The magnitude of the steric hindrance that we have found in our model MMOH_Q complex in the case of methane oxidation will surely not be quantitatively reliable for the actual MMOH_Q system in the enzymatic reaction in vivo. For such a quantitative determination, detailed knowledge of the pocket where CH₄ attacks, with its more bulky protein residues, would be required, and the effects of the dynamics should also be taken into account. Our study does not aim at the biological system but is certainly relevant for biomimetic dinuclear systems. The importance of the steric effects was recently highlighted by Shaik et al.⁴⁹ for the mononuclear [tmg₃trenFe^{IV}O]²⁺ complex with a *S* = 2 ground state, which had been prepared by Que and co-workers.⁵⁰ Steric hindrance effects, which may be tuned by variation of the ligands, will play a crucial role in enhancing the selectivity for methane oxidation in a dinuclear complex analogous to the one studied here. The FeO²⁺ group is a strong oxidant, also when dimerized in the Fe–O–O–Fe diamond core, and oxidation activity may be found in biomimetic complexes for a range of substrates, but the activity for bulkier substrates may be reduced significantly compared to methane by the proper choice of the ligands, taking the place of the formates in our model system.

AUTHOR INFORMATION

Corresponding Author

*E-mail: e.j.baerends@vu.nl.

Notes

[†]Dedicated to Professor Eluvathingal D. Jemmis on the occasion of his 60th birthday.

ACKNOWLEDGMENTS

The authors are indebted to the Dutch National Research School Combination “Catalysis Controlled by Chemical Design” (NRSC-Catalysis) for continuing financial support. We also acknowledge the computer time provided by the NWO Foundation for National Computing Facilities on the

Huygens and LISA at SARA, Amsterdam. The work was also supported by the World Class University program of the Korea Science and Engineering Foundation funded by the Ministry of Education, Science and Technology (Project R32-2008-000-10180-0).

REFERENCES

- (1) Meunier, B.; de Visser, S. P.; Shaik, S. *Chem. Rev.* **2004**, *104*, 3947–3980.
- (2) Schöneboom, J. C.; Cohen, S.; Lin, H.; Shaik, S.; Thiel, W. *J. Am. Chem. Soc.* **2004**, *126*, 4017–4034.
- (3) (a) Bassan, A.; Blomberg, M. R. A.; Borowski, T.; Siegbahn, P. E. M. *J. Inorg. Biochem.* **2006**, *100*, 727–743. (b) Krebs, C.; Fujimori, D. G.; Walsh, C. T.; Bollinger, J. M. *Acc. Chem. Res.* **2007**, *40*, 484–492.
- (4) Nam, W. *Acc. Chem. Res.* **2007**, *40*, 522–531.
- (5) (a) Buda, F.; Ensing, B.; Gribnau, M.; Baerends, E. J. *Chem.—Eur. J.* **2001**, *7*, 2775–2783. (b) Ensing, B.; Buda, F.; Blöchl, P.; Baerends, E. J. *Angew. Chem., Int. Ed.* **2001**, *40*, 2893–2895. (c) Ensing, B.; Buda, F.; Gribnau, M. C. M.; Baerends, E. J. *J. Am. Chem. Soc.* **2004**, *126*, 4355–4365.
- (6) (a) Yoshizawa, K.; Yumura, T.; Shiota, Y.; Yamabe, T. *Bull. Chem. Soc. Jpn.* **2000**, *73*, 29–36. (b) Yang, G.; Zhou, D.; Liu, X.; Han, X.; Bao, X. *J. Mol. Struct.* **2006**, *797*, 131–139. (c) Rosa, A.; Ricciardi, G.; Baerends, E. J. *Inorg. Chem.* **2010**, *49*, 3866–3880.
- (7) (a) Decker, A.; Clay, M. D.; Solomon, E. I. *J. Inorg. Biol. Chem.* **2006**, *100*, 697–706. (b) Louwse, M. J.; Baerends, E. J. *Phys. Chem. Chem. Phys.* **2007**, *9*, 156–166. (c) Hirao, H.; Que, L. Jr.; Nam, W.; Shaik, S. *Chem.—Eur. J.* **2008**, *14*, 1740–1756.
- (8) Michel, C.; Baerends, E. J. *Inorg. Chem.* **2009**, *48* (8), 3628–3638.
- (9) (a) Bernasconi, L.; Louwse, M. J.; Baerends, E. J. *Eur. J. Inorg. Chem.* **2007**, 3023–3033. (b) Shaik, S.; Hirao, H.; Kumar, D. *Acc. Chem. Res.* **2007**, *40*, 532–542. (c) Hirao, H.; Kumar, D.; Que, L. Jr.; Shaik, S. *J. Am. Chem. Soc.* **2006**, *128*, 8590–8606. (d) Hirao, H.; Kumar, D.; Thiel, W.; Shaik, S. *J. Am. Chem. Soc.* **2005**, *127*, 13007–13018.
- (10) (a) Siegbahn, P. E. M.; Blomberg, M. R. A. *Chem. Rev.* **2000**, *100*, 421–437. (b) Himo, F.; Siegbahn, P. E. M. *Chem. Rev.* **2003**, *103*, 2421–2456. (c) Siegbahn, P. E. M.; Borowski, T. *Acc. Chem. Res.* **2006**, *39*, 729–738. (d) Siegbahn, P. E. M.; Crabtree, R. H. *Struct. Bonding (Berlin)* **2000**, *97*, 125–144. (e) Blomberg, M. R. A.; Siegbahn, P. E. M. *J. Phys. Chem. B* **2001**, *105*, 9375–9386.
- (11) (a) Anthony, C. *The Biochemistry of Methylophilic; Academic Press*: London, 1982. (b) Hanson, R. S.; Hanson, T. E. *Microbiol. Rev.* **1996**, *60*, 439–471.
- (12) Solomon, E. I.; Sundaram, U. M.; Machonkin, T. E. *Chem. Rev.* **1996**, *96*, 2563–2605.
- (13) Que, L.; Dong, Y. H. *Acc. Chem. Res.* **1996**, *29*, 190–196.
- (14) Higgins, I. J.; Best, D. J.; Hammond, R. C. *Nature* **1980**, *286*, 561–564.
- (15) Gradassi, M. J.; Green, N. W. *Fuel Process. Technol.* **1995**, *42*, 65–83.
- (16) (a) Periana, R. A.; Taube, D. J.; Evitt, E. R.; Löffler, D. G.; Wentreck, P. R.; Voss, G.; Masuda, T. *Science* **1993**, *259*, 340–343. (b) Shilov, A. E.; Shul’pin, G. B. *Chem. Rev.* **1997**, *97*, 2879–2932.
- (17) Sorokin, A. B.; Kudrik, E. V.; Bouchu, D. *Chem. Commun.* **2008**, 2562–2564.
- (18) Murrell, J. C.; Gilbert, B.; McDonald, I. R. *Arch. Microbiol.* **2000**, *173*, 325–332.
- (19) Murrell, J. C. *Biodegradation* **1994**, *5*, 145–159.
- (20) Merckx, M.; Kopp, D. A.; Sazinsky, M. H.; Blazyk, J. L.; Müller, J.; Lippard, S. J. *Angew. Chem., Int. Ed.* **2001**, *40*, 2782–2807.
- (21) Miyaji, A.; Kamachi, T.; Okura, I. *Biotechnol. Lett.* **2002**, *24*, 1883–1887.
- (22) Xin, J. Y.; Cui, J. R.; Hu, X. X.; Li, S. B.; Xia, C. G.; Zhu, L. M.; Wang, Y. Q. *Biochim. Biophys. Res. Commun.* **2002**, *295*, 182–186.
- (23) Nguyen, H. H. T.; Elliott, S. J.; Yip, J. H. K.; Chan, S. I. *J. Biol. Chem.* **1998**, *273*, 7957–7966.

- (24) Fox, B. G.; Froland, W. A.; Lee, S.-K.; Lipscomb, J. D. *New J. Chem.* **1989**, *264*, 10023–10033.
- (25) Colby, J.; Dalton, H. *Biochem. J.* **1978**, *171*, 461–468.
- (26) Woodland, M. P.; Dalton, H. *J. Biol. Chem.* **1984**, *259*, 53–59.
- (27) Gassner, G. T.; Lippard, S. J. *Biochemistry* **1999**, *38*, 12768–12785.
- (28) Baik, M.-H.; Newcomb, M.; Friesner, R. A.; Lippard, S. J. *Chem. Rev.* **2003**, *103*, 2385–2419.
- (29) Liu, K. E.; Valentine, A. M.; Wang, D.; Huynh, B. H.; Edmondson, D. E.; Salifoglou, A.; Lippard, S. J. *J. Am. Chem. Soc.* **1995**, *117*, 10174–10185.
- (30) Liu, K. E.; Wang, D.; Huynh, B. H.; Edmondson, D. E.; Salifoglou, A.; Lippard, S. J. *J. Am. Chem. Soc.* **1994**, *116*, 7465–7466.
- (31) Brazeau, B. J.; Lipscomb, J. D. *Biochemistry* **2000**, *39*, 13503–13515.
- (32) Shu, L.; Nesheim, J. C.; Kauffmann, K.; Münck, E.; Lipscomb, J. D.; Que, L. *J. Science* **1997**, *275*, 515–518.
- (33) (a) Yoshizawa, K. *Acc. Chem. Res.* **2006**, *39*, 375–382. (b) Yoshizawa, K. *Coord. Chem. Rev.* **2002**, *226*, 251–259. (c) Yoshizawa, K. *J. Biol. Inorg. Chem.* **1998**, *3*, 318–324.
- (34) (a) Musaev, D. G.; Basch, H.; Morokuma, K. *J. Am. Chem. Soc.* **2002**, *124*, 4135–4144. (b) Basch, H.; Mogi, K.; Musaev, D. G.; Morokuma, K. *J. Am. Chem. Soc.* **1999**, *121*, 7249–7256. (c) Torrent, M.; Musaev, D. G.; Basch, H.; Morokuma, K. *J. Comput. Chem.* **2002**, *23* (1), 59–76.
- (35) (a) Friesner, R. A.; Dunietz, B. D. *Acc. Chem. Res.* **2001**, *34*, 351–358. (b) Guallar, V.; Gherman, B. F.; Lippard, S. J.; Friesner, R. A. *Curr. Opin. Chem. Biol.* **2002**, *6*, 236–242. (c) Friesner, R. A.; Baik, M. H.; Gherman, B. F.; Guallar, V.; Wirstam, M.; Murphy, R. B.; Lippard, S. J. *Coord. Chem. Rev.* **2003**, *238*, 267–290. (d) Baik, M. H.; Gherman, B. F.; Friesner, R. A.; Lippard, S. J. *J. Am. Chem. Soc.* **2002**, *124*, 14608–14615.
- (36) (a) Perdew, J. P.; Burke, K.; Ernzerhof, M. *Phys. Rev. Lett.* **1996**, *77*, 3865–3868. (b) Cohen, A. J.; Handy, N. C. *Mol. Phys.* **2001**, *99*, 607–615.
- (37) (a) Baerends, E. J.; Ellis, D. E.; Ros, P. *Chem. Phys.* **1973**, *2*, 41–51. (b) Velde, G. T.; Bickelhaupt, F. M.; Baerends, E. J.; Guerra, C. F.; Van Gisbergen, S. J. A.; Snijders, J. G.; Ziegler, T. *J. Comput. Chem.* **2001**, *22*, 931–967. (c) SCM. *ADF 2008.01*; Theoretical Chemistry, Vrije Universiteit: Amsterdam, The Netherlands, 2008; <http://www.scm.com/>.
- (38) (a) van Lenthe, E.; Baerends, E. J.; Snijders, J. G. *J. Chem. Phys.* **1994**, *101*, 9783–9792. (b) van Lenthe, E.; Baerends, E. J. *J. Chem. Phys.* **1999**, *110*, 8943–8953.
- (39) (a) Bernasconi, L.; Baerends, E. J. *Inorg. Chem.* **2009**, *48*, 527–540. (b) Rosa, A.; Ricciardi, G.; Baerends, E. J. *Inorg. Chem.* **2010**, *49*, 3866–3880.
- (40) (a) Swart, M.; Ehlers, A.; Lammertsma, K. *Mol. Phys.* **2004**, *102*, 2467–2474. (b) Swart, M. *J. Chem. Theor. Comput.* **2008**, *4* (12), 2057–2066. (c) Conradie, J.; Ghosh, A. *J. Chem. Theor. Comput.* **2007**, *3*, 689–702. (d) Schultz, N. E.; Zhao, Y.; Truhlar, D. G. *J. Phys. Chem. A* **2005**, *109*, 11127–11143. (e) Schultz, N. E.; Gherman, B. F.; Cramer, C. J.; Truhlar, D. G. *J. Phys. Chem. B* **2006**, *110*, 24030–24046. (f) Han, W. G.; Noodleman, L. *Inorg. Chem.* **2008**, *47*, 2975–2986.
- (41) (a) Handy, N. C.; Cohen, A. J. *Mol. Phys.* **2001**, *99*, 403–412. (b) Perdew, J. P.; Burke, K.; Ernzerhof, M. *Phys. Rev. Lett.* **1996**, *77*, 3865–3868. (c) Lee, C. T.; Yang, W.; Parr, R. G. *Phys. Rev. B* **1988**, *37*, 785–789.
- (42) Ahlrichs, R.; Bär, M.; Häser, M.; Horn, H.; Kölmel, C. *Chem. Phys. Lett.* **1989**, *162*, 165–169.
- (43) Solomon, E. I.; Decker, A.; Lehnert, N. *Proc. Natl. Acad. Sci. U.S.A.* **2003**, *100*, 3589–3594.
- (44) Belanzoni, P.; Bernasconi, L.; Baerends, E. J. *J. Phys. Chem. A* **2009**, *113*, 11926–11937.
- (45) Bickelhaupt, F. M.; Baerends, E. J. *Reviews in Computational Chemistry*; Lipkowitz, K. B., Boyd, D. R., Ed.; John Wiley: New York, 2000; Vol. 15, pp 1–86.
- (46) (a) Bickelhaupt, F. M.; Baerends, E. J.; Nibbering, N. M. M.; Ziegler, T. *J. Am. Chem. Soc.* **1993**, *115*, 9160–9173. (b) Diefenbach, A.; de Jong, G. Th.; Bickelhaupt, F. M. *Mol. Phys.* **2005**, *103*, 995–998. (c) de Jong, G. Th.; Bickelhaupt, F. M. *Chem. Phys. Chem.* **2007**, *8*, 1170–1181. (d) van Zeist, W.-J.; Bickelhaupt, F. M. *Org. Biomol. Chem.* **2010**, *8*, 3118–3127.
- (47) Louwse, M. J.; Vassilev, P.; Baerends, E. J. *J. Phys. Chem. A* **2008**, *112*, 1000–1012.
- (48) Michel, C.; Belanzoni, P.; Gamez, P.; Reedijk, J.; Baerends, E. J. *Inorg. Chem.* **2009**, *48* (24), 11909–11920.
- (49) Janardanan, D.; Wang, Y.; Schyman, P.; Que, L. Jr.; Shaik, S. *Angew. Chem., Int. Ed.* **2010**, *49*, 3342–3345.
- (50) England, J.; Martinho, M.; Farquhar, E. R.; Frisch, J. R.; Bominaar, E. L.; Münck, L.; Que, L. Jr. *Angew. Chem., Int. Ed.* **2009**, *48*, 3622–3636.